Progress in
Medical Devices

Zentime

RESEARCH ARTICLE

Design and analysis of a tissue retraction manipulator for neuroendoscopic surgery

Yu Liu, Gengqiang Shi

School of Health Sciences and Engineering, University of Shanghai for Science and Technology, Shanghai 200082, China.

Corresponding author: Gengqiang Shi.

Address correspondence to: Gengqiang Shi, School of Health Sciences and Engineering, University of Shanghai for Science and Technology, No. 334, Jungong Road, Yangpu District, Shanghai 200082, China.
E-mail: gengersgq@163.com.

Received October 24, 2025; Accepted January 8, 2026; Published March 24, 2026

DOI: 10.61189/091501wgyqdc

Abstract

This paper presents the design and analysis of a compact, cable-driven manipulator specifically for tissue retraction during neuroendoscopic surgery. The manipulator features an underactuated mechanism with a three-joint serial configuration, enabling stable motion within a single plane. Its compact design facilitates seamless integration into standard neuroendoscopic working channels, thereby optimizing spatial efficiency. The kinematic model was established using the Denavit-Hartenberg parameter method, with both forward and inverse kinematics systematically derived. Furthermore, a statics model was developed based on the Lagrangian formulation. Workspace analysis and trajectory planning were performed using Monte Carlo simulations in MATLAB. The simulation results indicate that the manipulator exhibits a feasible crescent-shaped workspace (X∈[10, 50.9] mm, Y∈[5.3, 44.9] mm). The motion trajectories of all joints were observed to be continuous and smooth, without any abrupt changes. Subsequent validation through ADAMS simulations confirmed the smooth variation of joint torques. This study provides a theoretical foundation and offers practical insights for the development and precise control of specialized instruments for neuroendoscopic surgery.

Keywords: Neuroendoscopic manipulator, Cable drive, Kinematic analysis, Simulation

1 INTRODUCTION

Neuroendoscopic surgery, a representative technique in modern minimally invasive neurosurgery, plays a vital and increasingly important role in treating intracranial lesions, owing to its significant advantages such as minimal trauma, rapid recovery, and short hospital stays [1, 2]. This technique involves advancing an endoscope and its working channel through narrow natural body cavities or micro-cranial bone windows to reach deep intracranial target areas, thereby providing surgeons with internal illumination and real-time visualization while minimizing damage to normal tissue [3, 4]. Precise and safe retraction or displacement of soft tissues—such as nerves and blood vessels—that obstruct the surgical field is critical for exposing key operative areas, preventing accidental injury, and ensuring surgical success [5]. However, neuroendoscopic surgery necessitates multi-handed manipulation by the surgeon. The highly minimally invasive nature of the procedure imposes severe spatial constraints, leading to significant interference between instruments [6]. Specifically, the manipulation of multiple instruments through the same channel frequently results in collisions, which severely compromises operational efficiency and safety [7, 8]. Surgeons therefore rely on handheld mechanical instruments to achieve stable and controllable tissue retraction or elevation.

To overcome the limitations of instruments in confined spaces, surgical robotics is considered a highly promising solution [9-11]. Commercialized laparoscopic surgical robots, such as the da Vinci SP system, demonstrate superior performance in larger cavities like the abdominal cavity through the introduction of wristed instruments [12-15]. However, their relatively large size makes them less suitable for minimally invasive procedures under strict spatial constraints. Consequently, research

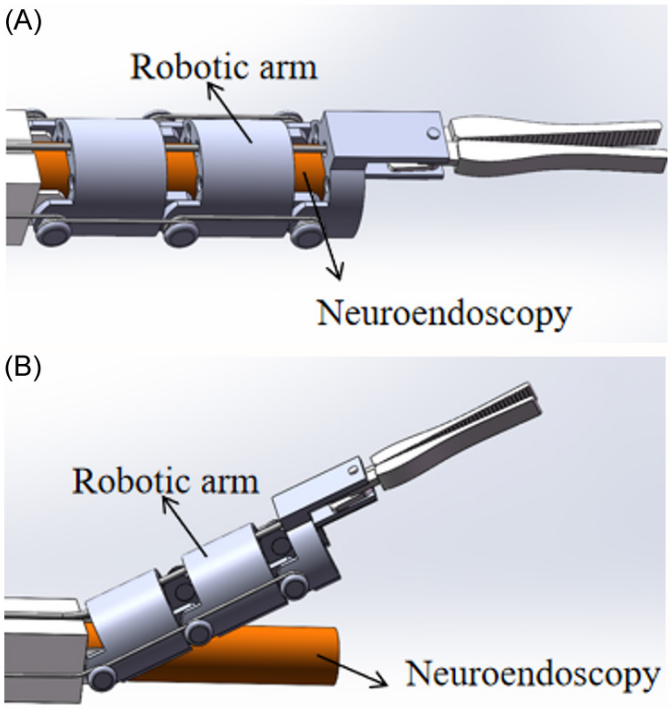

Figure 1. Schematic diagram of the mechanical hand structure model. (A) Retracted state; (B) Equivalent configuration during traction.

in this field has focused on highly flexible continuum robot designs [16-18].

Research efforts have explored various designs. For instance, a team from Incheon National University in South Korea developed a memory alloy-driven micro-flexible surgical robot [19]. Researchers at Shandong University developed a cable-driven surgical puncture robot, while Chinese scholars Luo et al. investigated a pneumatic/wire-driven continuum surgical robot for natural orifice surgery [20, 21]. A team from the Harbin Institute of Technology designed a magnetically driven millimeter-scale continuum robot for human lumen surgery [22]. A key challenge in the current research landscape is balancing the dexterity, size, stiffness, drive efficiency, and control complexity of such instruments. Practical devices specifically tailored for human body channels have yet to achieve significant breakthroughs. Among these diverse technical approaches, cable-driven systems are predominant in ultra-compact surgical instrument design due to their highly miniaturizable structure, immunity to electromagnetic interference, and ability to transmit power over long distances [23, 24]. However, many existing systems prioritize a high number of degrees of freedom, which often leads to excessive complexity without optimizing for core tasks such as planar tissue retraction in neuroendoscopic surgery. Building upon prior research, this paper introduces a specialized, compact, cable-driven manipulator specifically designed for planar tissue retraction in neuroendoscopic surgery. The Denavit–Hartenberg (D-H) parameter method and Monte Carlo simulations were employed to analyze the manipulator's forward and inverse kinematics and its effective workspace, thereby validating the rationality and effectiveness of the overall design. Motion trajectory planning simulations conducted in MATLAB further verified the motion continuity of the manipulator.

2 OVERALL STRUCTURE OF THE MANIPULATOR

2.1 Cable tension relationship analysis

To ensure stability and motion continuity, the manipulator employs an underactuated design [25]. This design features a minimalist joint topology consisting of three rotational joints arranged in a serial linkage configuration: a proximal finger pitch joint, a middle finger pitch joint, and an end-effector pitch/gripping joint (which provides tissue grasping/release functionality). The joint motion is constrained to a single plane, maximizing spatial efficiency. This approach addresses the critical requirement for surgical field exposure in neuroendoscopy while avoiding the complexity and spatial inefficiency associated with redundant degrees of freedom. All joint motions are actuated by a compact cable-driven system, ensuring a simple mechanical structure that can be integrated directly into the standard working channel of a neuroendoscope. Pitch motion is generated by winding cables around fixed pulleys located on both sides of each joint. Grasping and releasing functions of the gripping joint are operated by cables pulled through the central aperture of the joint. The cables are guided from the proximal end and routed counterclockwise over the fixed pulleys to drive the three joints. The gripping joint is secured by winding cables around its dissection aperture, as shown in **Figure 1**.

The rotation angle of each joint is determined by the length of cable being pulled. In the neutral position, the length of cable wrapped around each fixed pulley equals the pulley's circumference. During rotation, the angular displacement corresponds to the arc length of the cable released, as shown in **Figure 2**. The relationship between joint angle and cable length is established through the following geometric derivation:

$$S = R \cdot \theta_1 \tag{1}$$

Applying the arc angle conversion formula yields:

$$\theta_2 = \theta_1 \cdot \frac{180}{\pi} \tag{2}$$

Where θ_1 is the angle of arc displacement, S is the arc length, R is the radius of the fixed pulley, and θ_2 is the angle of the center circle.

Consequently, the relationship between the center circle angle and cable length variation is expressed as:

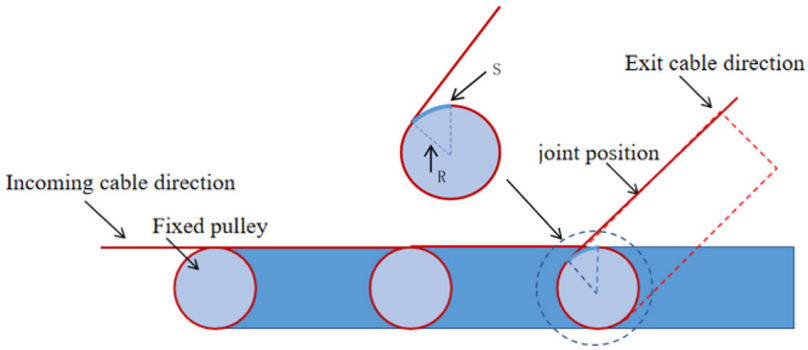

Figure 2. Schematic diagram of the cable joint tension relationship.

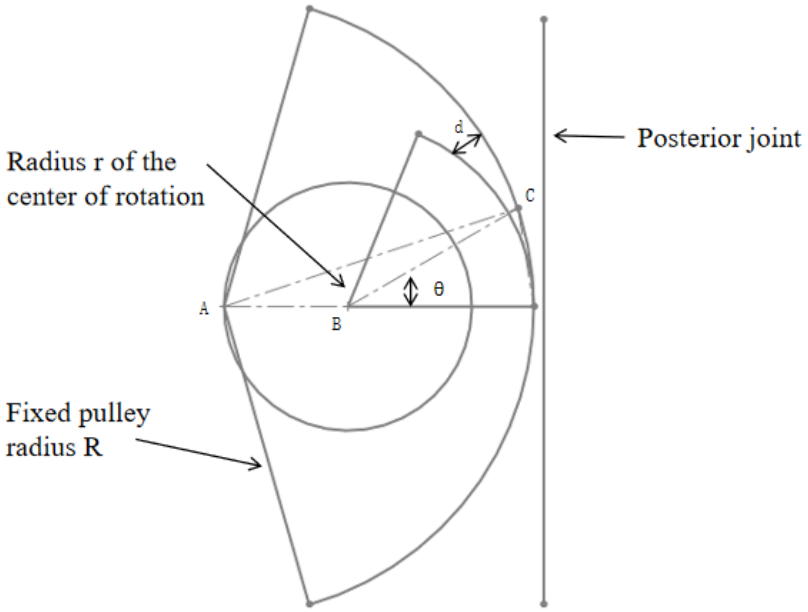

Figure 3. Schematic diagram of the design of the maximum angle of the joint.

$$S = R \cdot \theta_2 \cdot \frac{\pi}{180} \tag{3}$$

2.2 Maximum joint angle analysis

The maximum rotation angle θ for each joint is designed to be 30°, representing the ideal range of motion obtained through kinematic calculation. Due to an offset between the center of the arc at the joint end and the center of the fixed pulley, a specific clearance distance maintained between adjacent joints leads to a displacement during rotation. When this displacement equals the clearance at the rear joint, the two joints undergo rigid collision, halting rotation.

As shown in **Figure 3**, by constructing triangle ABC and applying trigonometric relations, the following is obtained:

$$AC^2 = AB^2 + BC^2 - AB \cdot BC \cdot \cos(\pi - \theta) \tag{4}$$

Solving equation (4) yields:

$$R^2 = (R - r)^2 + (r + d)^2 - (R - r) \cdot (r + d) \cdot \cos(\pi - \theta) \tag{5}$$

Equation (5) indicates that for given radii of the joint arc and the fixed pulley, the maximum angle θ before collision occurs is governed by the clearance distance d. Thus, the maximum angle θ can be optimally designed by appropriately adjusting the clearance distance.

3 KINEMATIC ANALYSIS OF THE MANIPULATOR

The kinematics of the three finger joints, which bend under cable tension, are analyzed using the standard D-H parameter method to model the relationship between their range of motion and configuration changes. The parameter coordinate systems between the manipulator's joints are shown in **Figure 4**. The D-H parameters and corresponding joint ranges of motion for the manipulator are listed in **Table 1**.

3.1 Forward kinematics

Forward kinematics provides the foundation for robotic motion control and path planning, involving the mathematical derivation of the end-effector pose from a given set of joint angles. It establishes the transformation between the robot's base frame and the end-effector frame using a 4×4 homogeneous transformation matrix. This section presents forward and inverse kinematic analyses of the manipulator based on the established D-H parameter model [26]. The overall transformation matrix is obtained by successively multiplying the transformation matrices of individual joints.

The transformation matrix between adjacent robot links is defined as:

$$^{i}_{i+1}T = Rot(z, \theta_{i+1}) \times Trans(0, 0, d_{i+1}) \times Trans(a_{i+1}, 0, 0) \times Rot(x, \alpha_{i+1}) \tag{6}$$

$$= \begin{bmatrix} C\theta_{i+1} & -S\theta_{i+1}C\alpha_{i+1} & S\theta_{i+1}S\alpha_{i+1} & \alpha_{i+1}C\theta_{i+1} \\ S\theta_{i+1} & C\theta_{i+1}C\alpha_{i+1} & -C\theta_{i+1}S\alpha_{i+1} & \alpha_{i+1}S\theta_{i+1} \\ 0 & S\alpha_{i+1} & C\alpha_{i+1} & d_{i+1} \\ 0 & 0 & 0 & 1 \end{bmatrix} \tag{7}$$

Where the following notation is used: cosθ=Cθ, sinθ=Sθ; cosα=Cα, sinα=Sα.

The joint rotation matrices, starting from the proximal joint, are as follows:

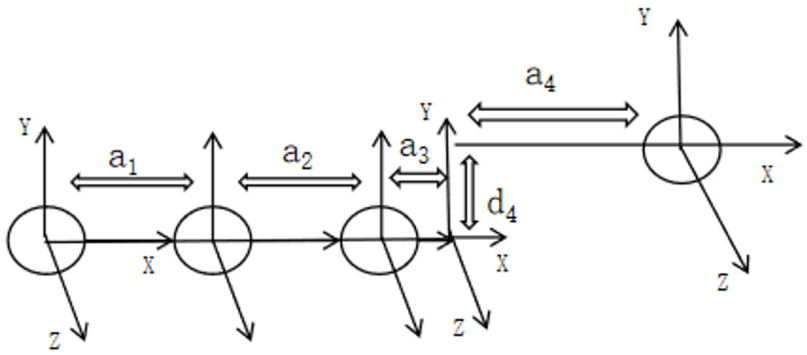

Figure 4. Denavit–Hartenberg coordinate diagram of the manipulator.

Table 1. Denavit–Hartenberg parameters of the manipulator

i	θ	d(mm)	α	a(mm)
1	$\theta_1(0,30^0)$	0	0	$a_1(10)$
2	$\theta_2(0,30^0)$	0	0	$a_2(10)$
3	$\theta_3(0,30^0)$	0	0	$a_3(5)$
4	$\theta_4(0)$	$d_4(4.5)$	0	$a_4(25)$

$$ {}^0_1T = \begin{bmatrix} C\theta_1 & -S\theta_1 & 0 & a_1C\theta_1 \\ S\theta_1 & C\theta_1 & 0 & a_1S\theta_1 \\ 0 & 0 & 1 & 0 \\ 0 & 0 & 0 & 1 \end{bmatrix} \tag{8} $$

$$ {}^1_2T = \begin{bmatrix} C\theta_2 & -S\theta_2 & 0 & a_2C\theta_2 \\ S\theta_2 & C\theta_2 & 0 & a_2S\theta_2 \\ 0 & 0 & 1 & 0 \\ 0 & 0 & 0 & 1 \end{bmatrix} \tag{9} $$

$$ {}^2_3T = \begin{bmatrix} C\theta_3 & -S\theta_3 & 0 & a_3C\theta_3 \\ S\theta_3 & C\theta_3 & 0 & a_3S\theta_3 \\ 0 & 0 & 1 & 0 \\ 0 & 0 & 0 & 1 \end{bmatrix} \tag{10} $$

The final homogeneous transformation matrix defines the pose of the end-effector's tip (gripping point) relative to the base frame:

$$ {}^3_4T = \begin{bmatrix} 1 & 0 & 0 & a4 \\ 0 & 1 & 0 & d4 \\ 0 & 0 & 1 & 0 \\ 0 & 0 & 0 & 1 \end{bmatrix} \tag{11} $$

Denoting the homogeneous transformation matrix of the end-effector gripping point as:

$$ {}^0_4T = \begin{bmatrix} n_x & o_x & a_x & p_x \\ n_y & o_y & a_y & p_y \\ n_z & o_z & a_z & p_z \\ 0 & 0 & 0 & 1 \end{bmatrix} \tag{12} $$

Based on the D-H method, overall transformation matrix for the end effector pose is obtained by concatenating the individual joint transformations:

$$ {}^0_4T = {}^0_1T \times {}^1_2T \times {}^2_3T \times {}^3_4T \tag{13} $$

The resulting elements of ${}^0_4T$ are:

$$ n_x = C\theta_{123}, o_x = -S\theta_{123}, a_x = 0, $$
$$ p_x = a_1C\theta_1 + a_2C\theta_{12} + a_3C\theta_{123} + a_4C\theta_{123} - d_4S\theta_{123}, $$
$$ n_y = S\theta_{123}, o_y = C\theta_{123}, a_y = 0, $$
$$ p_y = a_1S\theta_1 + a_2S\theta_{12} + a_3S\theta_{123} + a_4S\theta_{123} + d_4C\theta_{123}, $$
$$ n_z = 0, o_z = 0, a_z = 1, p_z = 0, $$

Where the abbreviated notation $C\theta_{ij}=cos(\theta_i+\theta_j)$, $S\theta_{ij}=sin(\theta_i+\theta_j)$ is used.

3.2 Inverse kinematics

The inverse kinematics analysis determines the rotational angles θ of each joint based on the homogeneous transformation matrix of the robot's end-effector joint pose, whose elements are given in Equation (12). This section uses the inverse transformation method to solve for the joint angles. The solution procedure is outlined as follows:

From Equation (13), we obtain:

$$ \theta_{123} = \arctan\frac{n_y}{n_x} \tag{14} $$

Order:

$$ p_x - a_3n_x - a_4n_x + d_4n_y = a_1C\theta_1 + a_2C\theta_{12} = K_x \tag{15} $$

$$ p_y - a_3n_x - a_4n_x - d_4n_y = a_1S\theta_1 + a_2S\theta_{12} = K_y \tag{16} $$

Available:

$$ \begin{aligned} &K_x^2 + K_y^2 = a_1^2 + a_2^2 + 2a_1a_2C\theta_2 \\ &= (p_x - a_3n_x - a_4n_x + d_4n_y)^2 + (p_y - a_3n_x - a_4n_x - d_4n_y)^2 \end{aligned} \tag{17} $$

Then the equation for θ_2 is:

$$ \theta_2 = arccos\frac{K_x^2 + K_y^2 - a_1^2 - a_2^2}{2a_1a_2} \tag{18} $$

Rewriting Equation (15)-(16) as:

$$\begin{aligned} K_x - a_1 C\theta_1 &= a_2 C\theta_{12} \\ K_y - a_1 S\theta_1 &= a_2 S\theta_{12} \end{aligned} \tag{19}$$

Squaring both sides of the equation and adding yields:

$$K_x C\theta_1 + K_y S\theta_1 = \frac{K_x^2 + K_y^2 + a_1^2 - a_2^2}{2a_1} \tag{20}$$

Define

$$\cos\varnothing = \frac{K_x}{\sqrt{K_x^2 + K_y^2}} \tag{21}$$

$$\sin\varnothing = \frac{K_y}{\sqrt{K_x^2 + K_y^2}} \tag{22}$$

So that

$$\varnothing = arctan\frac{K_y}{K_x} \tag{23}$$

Using trigonometric relationships, the expression for θ_1 is:

$$\sqrt{K_x^2 + K_y^2}\,(cos\varnothing cos\theta_1 + sin\varnothing sin\theta_1) = \frac{K_x^2 + K_y^2 + a_1^2 - a_2^2}{2a_1} \tag{24}$$

$$\theta_1 = \varnothing + arccos\frac{\frac{K_x^2 + K_y^2 + a_1^2 - a_2^2}{2a_1}}{\sqrt{K_x^2 + K_y^2}} \tag{25}$$

Then the equation for θ_3 is:

$$\theta_3 = arctan\frac{n_y}{n_x} - \theta_1 - \theta_2 \tag{26}$$

3.3 Static analysis

Based on the Lagrangian formulation for serial robotic arms, the dynamic equations of the finger mechanism are expressed as:

$$D(q)\ddot{q} + C(q,\dot{q}) + G(q) + \tau_f(\dot{q}) = \tau_t \tag{27}$$

Where $q=[\theta_1\ \theta_2\ \theta_3]^T$, $q, \dot{q}, \ddot{q}$ denote the angular displacement, velocity, and acceleration vectors of the finger joints; $D(q)$ is the inertia matrix; $C(q, \dot{q})$ represents the centrifugal and Coriolis torque terms; $G(q)$ is the gravitational torque; $\tau_f(\dot{q})$ denotes joint friction torque; τ_t is the joint driving torque.

The elements of these matrices are calculated based on the geometric and inertial parameters of the three links. Substituting these elements into Equation (27) yields the complete dynamic equations of the finger mechanism.

The three finger segments are denoted as link 1, link 2, and link 3, with masses m_1, m_2, m_3, and moments of inertia about their respective centers of mass.

The Lagrange method is employed to solve for the joint torques. The fundamental expression of the Lagrange equation is:

$$\frac{d}{dt}\left(\frac{\partial L}{\partial \dot{q}_i}\right) - \frac{\partial L}{\partial q_i} = \tau_t, i = 1,2,3 \tag{28}$$

In the equation, L represents the Lagrangian operator, where L=K-P, with K the total kinetic energy and P the total potential energy of the linkage system. To proceed, the linear velocities, accelerations, and angular accelerations of each link must be determined individually. Substituting the Lagrangian into equation (27) and performing differential calculations yields the corresponding torque matrix.

For link 1, the position of its center of mass in the coordinate system $O_1 X_1 Y_1 Z_1$ can be represented as ${}^1p_{r_1}=[r_1,0,0]^T$.

Rotating about the origin of the basis coordinate system with angular velocity $\dot{\theta}_1$, its linear velocity is $v_1 = r_1\dot{\theta}_1$.

The kinetic and potential energies of link 1 are respectively:

$$K_1 = \frac{1}{2}m_1 v_1^2 + \frac{1}{2}I_1\dot{\theta}_1^2 = \frac{1}{2}(m_1 r_1^2 + I_1)\dot{\theta}_1^2 \tag{29}$$

$$P_1 = m_1 g_1 r_1 S\theta_1 \tag{30}$$

For rod 2, its center of mass in the coordinate system $O_2 X_2 Y_2 Z_2$ can be expressed as ${}^2p_{r_2} = [r_2, 0, 0]^T$.

Through coordinate transformation, its position ${}^0p_{r_2}$ in the base coordinate system can be expressed as:

$${}^0p_{r_2} = {}^0A_1\,{}^1A_2\,{}^2p_{r_2} = \begin{bmatrix} l_1 C\theta_1 + r_2 C\theta_{12} \\ l_1 S\theta_1 + r_2 S\theta_{12} \\ 0 \end{bmatrix} \tag{31}$$

According to equation (31), the absolute velocity of the center of mass of rod 2 can be calculated as:

$$\frac{d^0p_{r_2}}{dt} = \begin{bmatrix} -l_1\dot{\theta}_1 S\theta_1 - r_2\dot{\theta}_{12}S\theta_{12} \\ l_1\dot{\theta}_1 C\theta_1 + r_2\dot{\theta}_{12}C\theta_{12} \\ 0 \end{bmatrix} \tag{32}$$

Accordingly, the kinetic energy K_2 of rod 2 can be determined as:

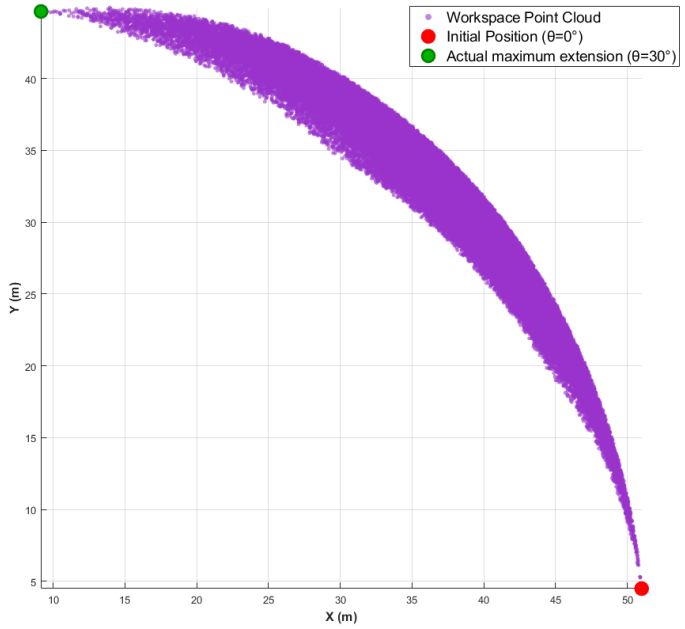

Figure 5. Workspace schematic of the robotic hand.

$$K_2 = \frac{1}{2} m_2 v_2^2 + \frac{1}{2} I_2 \dot{\theta}_2^2 \tag{33}$$

The linear velocity v_2 is:

$$v_2^2 = l_1^2 \dot{\theta}_1^2 + r_2^2 \dot{\theta}_{12}^{\ 2} + 2 l_1 r_2 \dot{\theta}_1 \dot{\theta}_{12} C\theta_2 \tag{34}$$

Potential energy P_2 is:

$$P_2 = m_2 g_2 \left[l_1 S\theta_1 + r_2 S\theta_{12} \right] \tag{35}$$

For rod 3, its center of mass in the coordinate system O_3-$X_3Y_3Z_3$ can be expressed as ${}^3p_{r_3}=[r_3,h_3,0]^T$.

Through coordinate transformation, its position ${}^0p_{r_2}$ in the base coordinate system can be expressed as:

$${}^0pr_3 = {}^0A_1 {}^1A_2 {}^2A_3 {}^3pr_3 = \begin{bmatrix} l_1 C\theta_1 + l_2 C\theta_{12} + r_3 C\theta_{123} - h_3 C\theta_{123} \\ l_1 S\theta_1 + l_2 S\theta_{12} + r_3 S\theta_{123} + h_3 C\theta_{123} \\ 0 \end{bmatrix} \tag{36}$$

According to equation (36), the absolute velocity of the center of mass of rod 2 can be calculated as:

$$\frac{d^0 pr_3}{dt} = \begin{bmatrix} -l_1 \dot{\theta}_1 S\theta_1 - l_2 \dot{\theta}_{12} S\theta_{12} - r_3 \dot{\theta}_{123} S\theta_{123} - h_3 \dot{\theta}_{123} C\theta_{123} \\ l_1 \dot{\theta}_1 C\theta_1 + l_2 \dot{\theta}_{12} C\theta_{12} + r_3 \dot{\theta}_{123} C\theta_{123} - h_3 \dot{\theta}_{123} S\theta_{123} \\ 0 \end{bmatrix} \tag{37}$$

Accordingly, the kinetic energy K_3 of rod 3 can be determined as:

$$K_3 = \frac{1}{2} m_3 v_3^2 + \frac{1}{2} I_3 \dot{\theta}_3^2 \tag{38}$$

The linear velocity v_3 is:

$$\begin{aligned} v_3^2 &= l_1^2 \dot{\theta}_1^2 + l_2^2 \dot{\theta}_{12}^2 + (r_3^2 + h_3^2) \dot{\theta}_{123}^2 + 2 l_1 l_2 \dot{\theta}_1 \dot{\theta}_{12} C\theta_2 \\ &+ 2 l_1 r_3 \dot{\theta}_1 \dot{\theta}_{123} C\theta_{23} - 2 l_1 h_3 \dot{\theta}_1 \dot{\theta}_{123} S\theta_{23} \\ &+ 2 l_2 r_3 \dot{\theta}_{12} \dot{\theta}_{123} C\theta_3 - 2 l_2 h_3 \dot{\theta}_{12} \dot{\theta}_{123} S\theta_3 \end{aligned} \tag{39}$$

Potential energy P_3 is:

$$P_3 = m_3 g_3 \left[l_1 S\theta_1 + l_2 S\theta_{12} + r_3 S\theta_{123} + h_3 C\theta_{123} \right] \tag{40}$$

Both the kinetic energy and potential energy of the linkage system have been determined, enabling the calculation of the Lagrangian operator:

$$L = K - P = K_1 + K_2 + K_3 - P_1 - P_3 - P_3 \tag{41}$$

Using the Lagrange operator L, calculate the partial derivatives for each joint variable: $\frac{\partial L}{\partial \theta_i}$, $\frac{\partial L}{\partial \dot{\theta}_i}$, $\frac{d}{dt}\frac{\partial L}{\partial \dot{\theta}_i}$, i=1,2,3.

Substituting the above results into the Lagrange equations (27) yields the joint torques.

4 ROBOTIC ARM SIMULATION ANALYSIS

The workspace of the manipulator was analyzed using the Monte Carlo method [27]. A large number of random joint angle combinations were generated within their allowable ranges, and the corresponding end-effector positions were computed via the forward kinematics model in MATLAB. The point cloud representing these positions was plotted to visualize the workspace. As shown in **Figure 5**, the robotic arm's motion range forms a crescent shape, with spatial extents of X∈(10, 50.9) mm and Y∈(5.3, 44.9) mm. This extensive motion range meets the practical movement requirements of each mechanical joint and effectively fulfills the design task of expanded traction.

Trajectory planning is a critical aspect of robotics, as it significantly influences the performance and smoothness of robotic motion. In this study, a point-to-point trajectory between specified initial and terminal poses was planned. The trajectory was generated using quintic polynomial interpolation via the MATLAB Robotics Toolbox, based on the established kinematic model. This process generated the angle, angular velocity, and angular acceleration profiles for the three joints along the planned path.

Starting pose:

$$\begin{bmatrix} 1 & 0 & 0 & 51.00 \\ 0 & 1 & 0 & 4.50 \\ 0 & 0 & 1 & 0 \\ 0 & 0 & 0 & 1 \end{bmatrix} \tag{42}$$

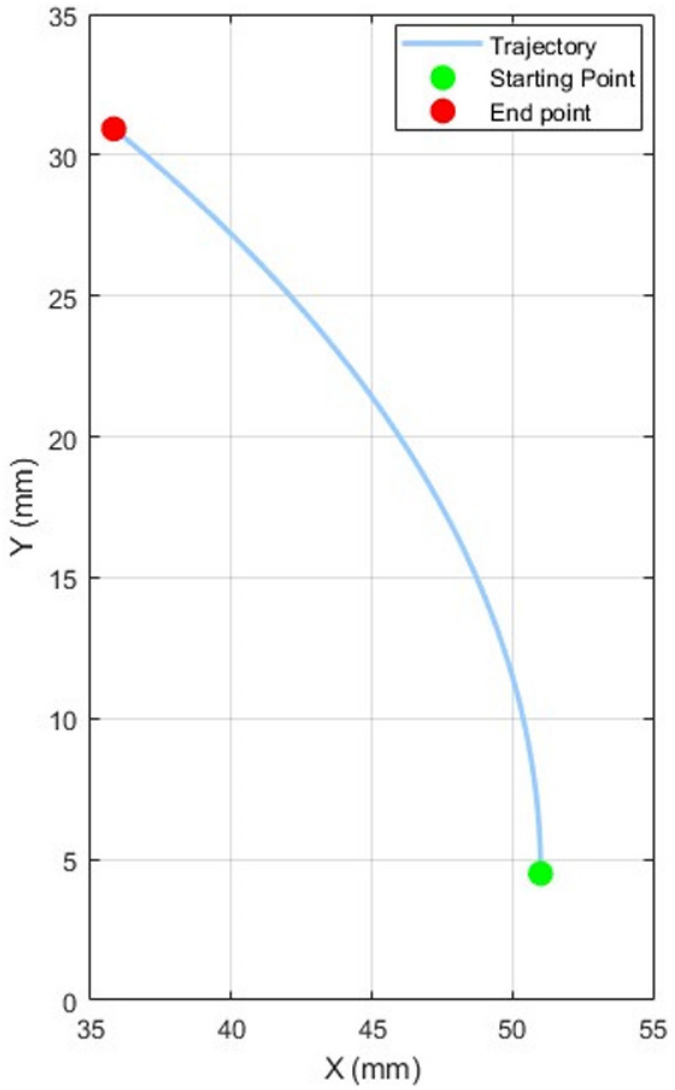

Figure 6. Trajectory planning results.

Terminal pose:

$$\begin{bmatrix} 0.642788 & -0.766044 & 0 & 35.84 \\ 0.766044 & 0.642788 & 0 & 30.93 \\ 0 & 0 & 1 & 0 \\ 0 & 0 & 0 & 1 \end{bmatrix} \quad (43)$$

The resulting trajectories are shown in **Figure 6**.

As illustrated in **Figures 7-9**, the angular displacement, velocity, and acceleration profiles of all three joints demonstrate smooth transitions without abrupt changes during motion along the planned trajectory. This finding indicates that all joints can be driven stably throughout the workspace, thereby validating the rationality of the mechanical design. The manipulator model developed in SOLIDWORKS was subsequently imported into ADAMS for dynamic simulation. Within the ADAMS environment, the material properties were defined as steel, and the corresponding joint torque profiles were acquired. Collectively, these simulation results provide an intuitive and practical reference for the subsequent development of the physical platform and the design of its control system.

As shown in **Figure 10**, the negative values on the Y-axis indicate only the direction of the torque, not its magnitude. The torque variation curve reveals that the torque at all three joints exhibits an approximately S-shaped continuous trend. The transitions are smooth and uniform, with no abrupt changes observed. This indicates that the load transition at each joint during motion is stable, meeting the design expectations and stability requirements.

5 CONCLUSION

This study addresses the practical need for tissue retraction in neuroendoscopic surgery by presenting the design of a compact, cable-driven manipulator tailored for minimally invasive procedures. The proposed manipulator employs an underactuated design with a minimalist three-joint topology, achieving stable planar motion. This configuration significantly reduces the spatial footprint while ensuring full functionality, thereby enabling seamless integration into standard neuroendoscopic working channels. This makes the manipulator particularly suitable for confined surgical environments.

In terms of mechanism design, the maximum joint rotation angle was mechanically constrained through the coordinated design of joint arcs and fixed pulleys, coupled with precise clearance control. A kinematic model was established based on the D-H parameter method, and the forward and inverse kinematic relationships were systematically derived. Furthermore, a static model was constructed using the Lagrange method, providing a theoretical foundation for control and force feedback. Trajectory planning analysis conducted in MATLAB demonstrated that the manipulator possesses a feasible crescent-shaped workspace, which is sufficient for the required traction and exposure of surgical sites. The combined results from the trajectory and torque simulations revealed continuous and smooth motion profiles for all joints, with no abrupt changes, further validating the rationality of the mechanism design and its motion stability.

While this study has made significant progress in structural design and kinematic analysis, several limitations remain to be addressed. For instance, the current model does not incorporate effects such as time delay and deformation caused by cable flexibility. Furthermore, the mechanical performance under extreme loading conditions requires further experimental vali-

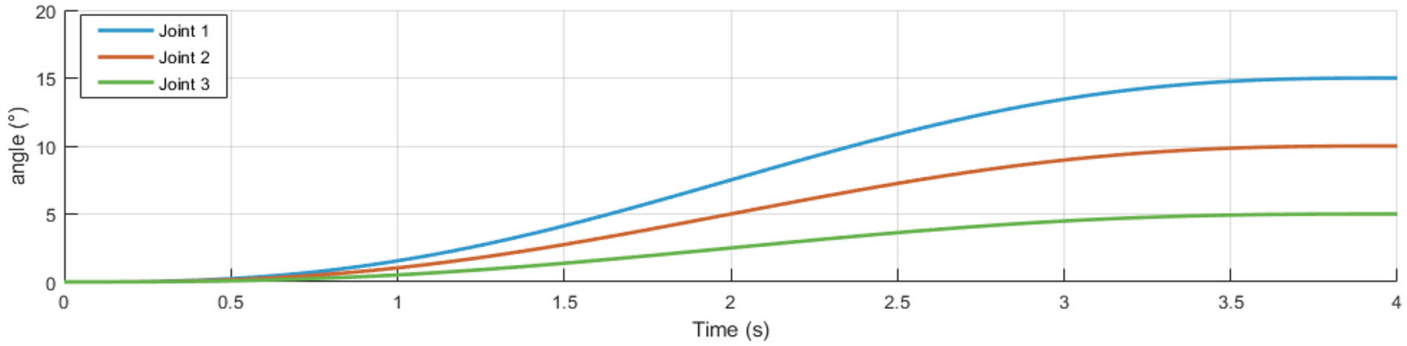

Figure 7. Joint angle profiles.

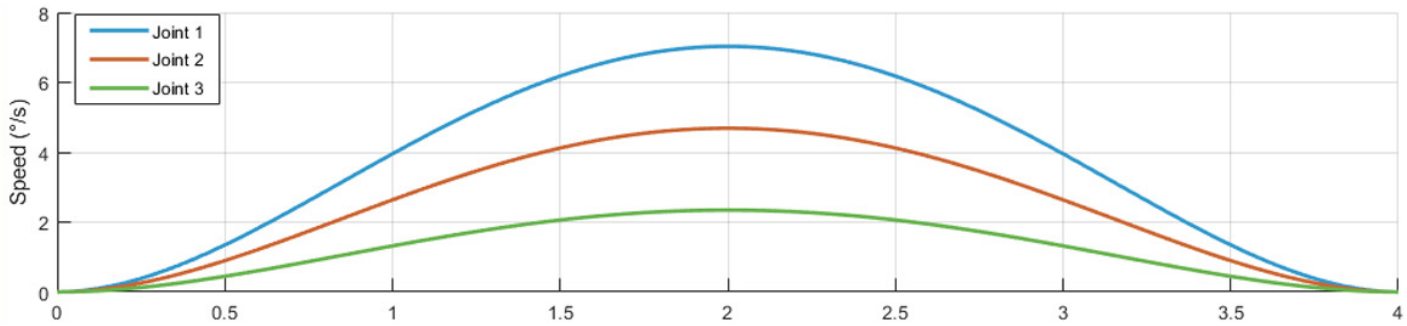

Figure 8. Joint angular velocity profiles.

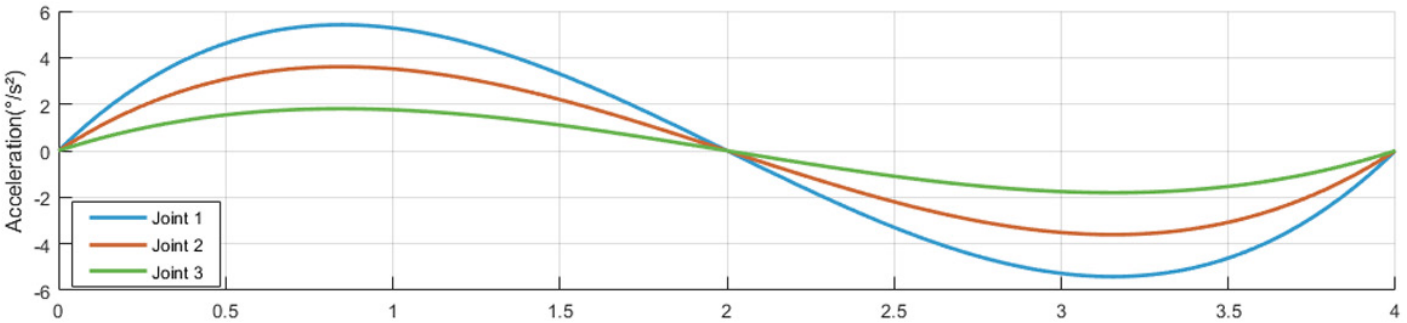

Figure 9. Joint angular acceleration profiles.

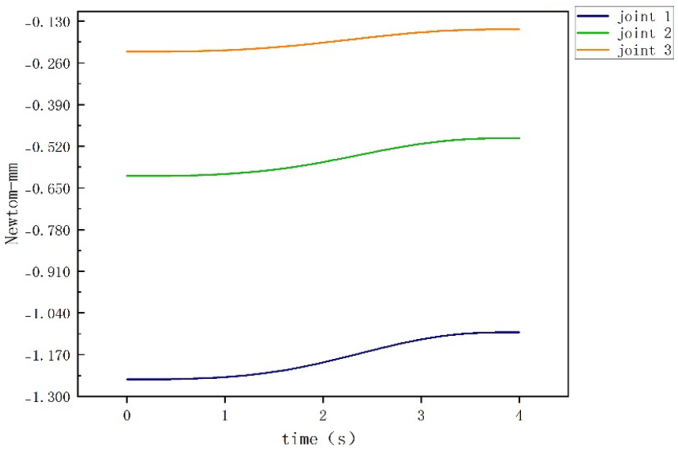

Figure 10. Joint torque profiles.

dation. Future work also includes coordinating the manipulator's motion with a robotic arm to achieve free movement in three-dimensional space, which warrants further investigation.

DECLARATIONS

Author contributions

Both authors contributed equally to the work. Liu participated in the implementation and drafting of the manuscript, while Shi contributed to the conceptual development and design of the study.

Funding

This research received no external funding.

Data availability

The data presented in this study are authentic and reliable.

Ethics approval and consent to participate

Not applicable (this study did not involve any procedures requiring ethical review).

Consent for publication

The submitted manuscript has not been published elsewhere (except in the form of an abstract or a conference presentation) and is not currently under consideration for publication by any other journal.

Competing interests

The authors declare no potential conflicts of interest with respect to the research, authorship, or publication of this article.

Acknowledgements

Not applicable.

REFERENCES

[1] Xu L, Lu X, Zhang C, Wang W. Clinical efficacy of neuroendoscopy combined with intracranial pressure monitoring for the treatment of hypertensive intracerebral hemorrhage. World Neurosurg. 2024 Jul;187:e210-e219. https://doi.org/10.1016/j.wneu.2024.04.068

[2] Banoci J, Magocova V, Katuch V, Tomkova M. Neuroendoscopy-assisted evacuation for supratentorial intracerebral hemorrhage versus conventional craniotomy: A comparative analysis of efficacy and outcome. Bratisl Lek Listy. 2024;125(12):775-779. https://doi.org/10.4149/bll_2024_118

[3] Wang L, Zhou T, Wang P, Zhang S, Yin Y, Chen L, et al. Efficacy and safety of neuroendoscopic surgery for intracerebral hemorrhage: A randomized, controlled, open-label, blinded endpoint trial (nesich). Int J Stroke. 2024 Jun;19(5):587-592. https://doi.org/10.1177/17474930241232292

[4] Zhou L, Jing X, Wang C, Zhang H, Lei P, Song P, et al. Clinical application of transcranial neuroendoscopy combined with supraorbital keyhole approach in minimally invasive surgery of the anterior skull base. Sci Rep. 2024 Jun 27;14(1):14886. https://doi.org/10.1038/s41598-024-65758-y

[5] Spennato P, Tengattini F, Picariello S, Gritti L, Porzio M, Ruggiero C, et al. The role of neuroendoscopy in treatment of pediatric brain abscesses: Case series and systematic review of the literature. Neurosurg Rev. 2025 Jun 20;48(1):518. https://doi.org/10.1007/s10143-025-03669-w

[6] Zhou L, Xu G, Liu K, Zhang H, Lei P, Lu M, et al. 3d slicer combined with neuroendoscopic surgery for the treatment of basal ganglia hemorrhage after cranioplasty: A case report and literature review. Heliyon. 2024 Sep 30;10(18):e37773. https://doi.org/10.1016/j.heliyon.2024.e37773

[7] Monteiro GA, Marinheiro G, Mutarelli A, Araújo B, Cavalcante-Neto JF, Batista S, et al. Efficacy and safety of neuroendoscopy surgery versus craniotomy for supratentorial intracerebral hemorrhage: An updated meta-analysis of randomized controlled trials. Neurosurg Rev. 2024 Jun 4;47(1):255. https://doi.org/10.1007/s10143-024-02492-z

[8] Waseem MH, Abideen ZU, Rehman N, Khan MH, Tahir MF, Raja HAA, et al. Efficacy and safety of neuroendoscopy versus craniotomy for spontaneous supratentorial intracerebral hemorrhage: An updated meta-analysis of randomized and non-randomized studies. Brain Behav. 2025 Sep;15(9):e70581. https://doi.org/10.1002/brb3.70581

[9] Omisore OM, Han S, Xiong J, Li H, Li Z, Wang L. A review on flexible robotic systems for minimally invasive surgery. IEEE Trans Syst Man Cybern Syst. 2022;52(1):631-644. https://doi.org/10.1109/TSMC.2020.3026174

[10] Shkurti TE, Çavuşoğlu MC. A systematic review of task automation in surgical robotics. IEEE Trans Med Robot Bionics. 2025;7(3):863-880. https://doi.org/10.1109/TMRB.2025.3583182

[11] Li C, Zhang G, Zhao B, Xie D, Du H, Duan X, et al. Advances of surgical robotics: Image-guided classification and application. Natl Sci Rev. 2024 Sep;11(9):nwae186. https://doi.org/10.1093/nsr/nwae186

[12] Park JI, Chung YK, Lee YM, Nam CW, Nah YW. Comparative analysis of postoperative outcomes of single-incision cholecystectomy: Propensity score matching of robotic surgery using the da Vinci SP system and da Vinci Xi system vs. laparoscopic surgery. Ann Hepatobiliary Pancreat Surg. 2025 May 31;29(2):140-149. https://doi.org/10.14701/ahbps.24-198

[13] Miyamura H, Takada K, Ohwaki A, Kobayashi A, Ito M, Nomura H, et al. Initial experience and surgical outcomes of robotic-assisted total hysterectomy using the da Vinci SP surgical system. Asian J Endosc Surg. 2024 Apr;17(2):e13298. https://doi.org/10.1111/ases.13298

[14] Heo JE, Han HH, Lee J, Choi YD, Jang WS. Single-port robot-assisted pyeloplasty using the da Vinci SP system versus multiport pyeloplasty: Comparison of outcomes and costs. Asian J Surg. 2024 Sep;47(9):3841-3846. https://doi.org/10.1016/j.asjsur.2024.03.175

[15] Vizza R, Corrado G, Mancini E, Baiocco E, Russo M, Vincenzoni C, et al. Feasibility, safety, and efficacy of robotic single-port hysterectomy (R-SPH) using the da Vinci SP system in low-risk endometrial cancer: A pilot study. Minim Invasive Ther Allied Technol. 2025 Dec;34(6):433-440. https://doi.org/10.1080/13645706.2025.2538764

[16] Wang Z, Weng D, Li Z, Chen L, Ma Y, Wang J. A magnetic-controlled flexible continuum robot with different deformation modes for vascular interventional navigation surgery. Actuators. 2023;12(6):247. https://doi.org/10.3390/act12060247

[17] Troncoso DA, Robles-Linares JA, Russo M, Elbanna MA, Wild S, Dong X, et al. A continuum robot for remote applications: From industrial to medical surgery with slender continuum robots. IEEE Robot Autom Mag. 2023;30(3):94-105. https://doi.org/10.1109/MRA.2022.3223220

[18] Sun L, Chen X. Flexible continuum robot system for minimally invasive endoluminal gastrointestinal endoscopy. Machines. 2024;12(6):370. https://doi.org/10.3390/machines12060370

[19] Jeon H, Le QN, Jeong S, Jang S, Jung H, Chang H, et al. Towards a snake-like flexible robot with variable stiffness using an sma spring-based friction change mechanism. IEEE Robot Autom Lett. 2022;7(3):6582-6589. https://doi.org/10.1109/LRA.2022.3174363

[20] Li J, Jiang Q. Optimal design and experiment of cable-driven puncturing surgery robot for soft needle. J Med Device. 2023 Feb 8;17:1-37. https://doi.org/10.1115/1.4056865

[21] Luo X, Song D, Zhang Z, Wang S, Shi C. A novel distal hybrid pneumatic/cable-driven continuum joint with variable stiffness capacity for flexible gastrointestinal endoscopy. Adv Intell Syst. 2023 Jun 1;5(6):2200403. https://doi.org/10.1002/aisy.202200403

[22] Mao L, Yang P, Tian C, Shen X, Wang F, Zhang H, et al. Magnetic steering continuum robot for transluminal procedures with programmable shape and functionalities. Nat Commun. 2024 May 4;15(1):3759. https://doi.org/10.1038/s41467-024-48058-x

[23] Zhang F, Fu Y, Yang L, Fu Y. A novel cable configuration method for fully-actuated parallel cable-driven systems: Application in a shoulder rehabilitation exoskeleton. Mech Mach Theory. 2024 Sep 1;199:105693. https://doi.org/10.1016/j.mechmachtheory.2024.105693

[24] Qin G, Cheng Y, Ji A, Pan H, Yang Y, Yao Z, et al. Research on the cable-driven endoscopic manipulator for fusion reactors. Nucl Eng Technol. 2024 Feb 1;56(2):498-505. https://doi.org/10.1016/j.net.2023.10.026

[25] Wu X, Li X, Li Z, Zhang D, Miao Z, Zhou J. An improved udwadia–kalaba approach for controller design in underactuated mechanical systems. Multibody Syst Dyn. 2025 Jun 1;64(2):195-218. https://doi.org/10.1007/s11044-024-10004-6

[26] Jia L, Liu S, Cao C, Kang Y, Zhu Y, Wang L, et al. Kinematics and spatial structure analysis of TBM gunite robot based on D-H parameter method. Sci Rep. 2024 Jun 13;14(1):13649. https://doi.org/10.1038/s41598-024-64439-0

[27] Yang Z, Tian W, Wang H, Liu X, Zhang D, Yan Y, et al. Snake-like robot workspace solving method based on improved monte carlo method. Appl Bionics Biomech. 2025;2025:6125695. https://doi.org/10.1155/abb/6125695